X-ray diffraction measurements and pressure determination in nanosecond compression of solids up to 600 GPa

F. Coppari [1,*] D. E. Fratanduono [1] M. Millot [1] R. G. Kraus [1] A. Lazicki,[1] J. R. Rygg [2,3,4]
R. F. Smith,[1] and J. H. Eggert[1]

[1]*Lawrence Livermore National Laboratory, Livermore, California 94550, USA*
[2]*Laboratory for Laser Energetics, University of Rochester, Rochester, New York 14627, USA*
[3]*Department of Mechanical Engineering, University of Rochester, Rochester, New York 14627, USA*
[4]*Department of Physics and Astronomy, University of Rochester, Rochester, New York 14627, USA*

X-ray diffraction measurements under laser-driven dynamic compression now allow us to investigate the atomic structure of matter at TPa pressures and thousands of degree temperatures, with broad implications for condensed matter physics, planetary science, and astronomy. Pressure determination in these experiments often relies on velocimetry measurements coupled with modeling that requires accurate knowledge of the optical and thermomechanical properties of a window material, resulting in significant systematic uncertainty. Here we report on a series of x-ray diffraction experiments on five metals dynamically compressed to 600 GPa. In addition to simultaneously collecting atomic structure information for multiple compressed samples, namely Pt, Ta, Au, W, and Fe, we demonstrate a different approach for pressure determination applicable to x-ray diffraction experiments under quasi-isentropic ramp compression. The method, based on the use of *in situ* pressure calibrants, is similar to the techniques often adopted in static compression with diamond anvil cells. Focusing on experiments using a diamond window, we discuss challenges and mitigation strategies for the novel approach. Our study provides lattice-level information on five different metals compressed to hundreds of GPa and validation to the currently used methods for pressure determination based on time-resolved measurement of the diamond free-surface velocity, revealing that the use of *in situ* calibrants enables a factor of four reduction in the pressure uncertainty in these experiments.

I. INTRODUCTION

The investigation of solids at extreme pressure and temperature conditions by laser-driven compression and *in situ* x-ray diffraction (XRD) measurements has seen a dramatic expansion in recent years. This technique, initially developed at kJ and MJ laser facilities, such as the Omega laser [1,2] (Rochester, NY) and more recently ORION [3] (UK), LULI [4] (France) and NIF [5] (Livermore, CA) among others, has now also been deployed at dedicated beamlines coupling 10–100J lasers with synchrotron radiation [6] and x-ray free electron lasers (XFEL) [7,8].

Similarly to gas gun or explosive drivers, $10^{13}-10^{15}$ W/cm², ns-long laser pulses can be used to generate single shock compression of materials to TPa pressure. However, shock compression induces significant heating causing melting near 0.1–0.5 TPa for most materials, thus limiting the pressure range over which the atomic structure of solids can be probed. In contrast, gradually increasing the laser power over multiple nanoseconds to generate a shockless or "ramp" compression allows us to achieve TPa pressures along quasi-isentropic paths, while maintaining the temperature below melting [9].

Here, we focus on a particular configuration used to produce ramp compression, in which a 1–10 µm thin sample is encapsulated between two 20–100-µm-thick single-crystal diamond plates (see Fig. 1). Provided that the increase in laser power is slow compared to the compression wave transit time through the sample, this approach enables wave reverberation between the two diamonds and results in a uniform pressure state within the whole thickness of the sample layer. The atomic structure of the compressed sample can then be probed with x-ray diffraction using a 1–2 ns flash of quasimonochromatic radiation.

This technique has been used to investigate structural stability, solid-solid phase transitions, melting and recrystallization of materials at conditions never accessed before in the laboratory. Evidence for pressure-induced phase transitions in minerals [10,11], metals [12,13], and molecular systems [14] and the exceptional stability of face-centered cubic Cu to 1 TPa [15] and of the diamond FC8 structure to 2 TPa [9] are but a few examples among the published results using these experimental methods.

In addition to the collection of XRD patterns, accurately determining the sample pressure during the x-ray exposure is critical to enable the comparison with theoretical models as well as with data obtained in different experiments. Most experiments to date rely on velocimetry measurements using VISAR (Velocity Interferometer System for Any Reflector) [16] to document the acceleration of the sample by recording
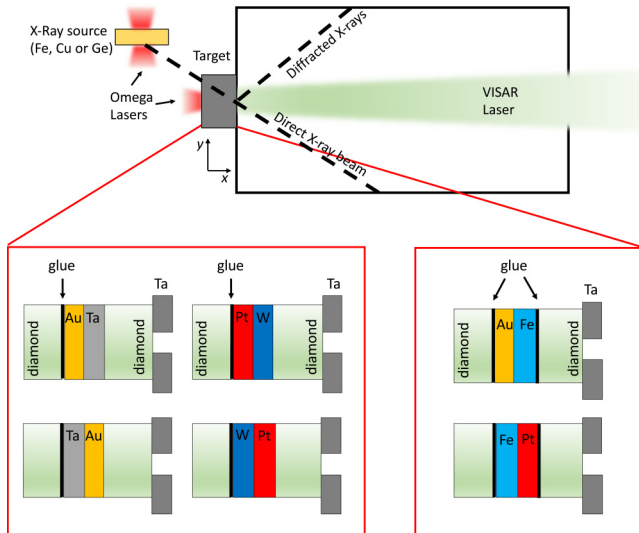
*coppari1@llnl.gov

FIG. 1. Schematic representation of the PXRDIP diagnostic used to measure x-ray diffraction during dynamic compression at the Omega Laser Facility [2,35] (not to scale). The sample (gray, with *x-y* coordinates indicated by arrows) is located on the front face of the diagnostic and the x-ray source ∼24 mm away at ∼45° (orange). The Omega and VISAR lasers are indicated in red and green and the direction of the transmitted and diffracted x-rays by black-dashed lines. The insets show the details of the different target configurations used in this study (not to scale).

the time history of the free-surface velocity of the diamond window over time. Inferring the sample compression from the velocity is not trivial and requires accurate knowledge of the optical and thermomechanical properties of diamond along the specific compression path of the experiment, resulting in significant systematic uncertainty.

In this paper, we collect and analyze new x-ray diffraction measurements of five metals dynamically compressed to hundreds of GPa. Using our data, we propose and validate a novel approach to pressure determination in x-ray diffraction experiments under dynamic ramp compression based on the collection of XRD patterns of *in situ* pressure calibrants. We ramp compress gold, tantalum, platinum, and tungsten and use their diffraction patterns to determine their density. Then, matching the practice commonly adopted in static compression experiments with diamond anvil cells (DAC) [17–19], we use the measured density of the calibrants to determine the pressure using previously calibrated pressure-density equation of state relationships.

We also illustrate the feasibility of this method performing x-ray diffraction and ramp-compression experiments on iron and discuss how the new approach compares with the current pressure determination relying on velocimetry measurements.

This approach offers a number of advantages, the most remarkable being a more precise pressure determination. Removing some of the systematic uncertainty associated with the current methods for pressure determination enables a better comparison with theoretical models for material properties at extreme conditions, as well as with data obtained in different experimental settings using both static and dynamic compression. This, in addition to advancing the experimental

technique, has the potential to improve our understanding of material behavior at high pressure with far-reaching consequences ranging from material science to geophysics and planetary science. This paper also represents a new capability for experiments at extreme pressures, where VISAR measurements may not be feasible, or for facilities where the VISAR diagnostic is not available. Benefits also extend to experiments at high-repetition rate, such as those performed at XFELs, by simplifying the data analysis workflow, since pressure and structure can be both determined by analyzing diffraction patterns, thus enabling optimized strategic decisions in a fast-paced data collection environment. Finally, this study also tackles issues related to sample preheating in laser-driven dynamic compression experiments.

II. CHALLENGES ASSOCIATED WITH CURRENT PRESSURE DETERMINATION METHODS

The use of diamond as ablator and window materials in reverberating ramp-compression and x-ray diffraction experiments has a number of advantages. Owing to the diamond stiffness, enclosing the material of interest between them ensures that fast reverberations take place and that the pressure in the sample equilibrates with the surrounding diamonds in a few nanoseconds. Diamond stiffness also makes it a good ablator, capable of sustaining and propagating quasi-isentropic compression [20]. Its low atomic number minimizes x-ray generation from laser ablation. Single crystal diamonds have a minimal and recognizable contribution to the diffraction signal (Supplemental Material in Refs. [10–12,14]) and no evidence for phase transitions has been reported upon ramp compression to 2 TPa [9]. Additionally, its pressure-density equation of state (EOS) and sound velocity have been measured up to 800 GPa along a quasi-isentropic compression path [21].

However, the use of diamond in these experiments also introduces complications and uncertainties. The strength of diamond, a quantity largely unknown upon compression and even more so upon release [22], heavily affects its pressure-density response [23] and has to be taken into account in order to correctly evaluate pressure. The limited knowledge of this important property under the loading path used in the specific experiment (ramp, shock, or release) increases the systematic uncertainties and affects our ability to obtain precise pressure determinations.

Additionally, diamond becomes opaque to the VISAR laser once compressed above the Hugoniot elastic limit (HEL, about 80 GPa [24]), which is the case for the vast majority of dynamic compression experiments. As a consequence the VISAR system does not probe the sample-diamond interface directly, but rather provides a free-surface velocity measurement, which requires either using the method of characteristics or radiation-hydrodynamic simulations in order to determine the pressure state of the sample. The method of characteristics (see Sec. IV for more details) requires that no shocks form into the sample [25]. Because the VISAR does not probe the interface motion, we cannot determine whether any shock-like feature in the velocity profile is due to shock formation into the sample or to ramp waves steepening during

propagation through the diamond window, possibly compromising the validity of the analysis framework.

These challenges call for validation of the currently used methods for pressure determination and possibly the development of alternative approaches.

III. APPROACH AND EXPERIMENTAL DETAILS

In order to validate and asses the performance of *in situ* pressure calibrants in dynamic ramp-compression x-ray diffraction measurements, we test different materials having different crystal structures. The sample in each experiment consists of a pair of coatings combining one with a face-centered cubic (fcc) structure with one body-centered cubic (bcc): either Au (fcc) with Ta (bcc) or Pt (fcc) with W (bcc). The choice of the material is dictated by the need to be a good scatterer, have low chemical reactivity, a simple crystal structure, no phase transitions, and a well-characterized pressure-density equation of state. High precision Au and Pt EOS are available from ramp-compression experiments at the National Ignition Facility [26] up to TPa pressure, making them good calibrants for reverberating ramp-compression experiments owing to the similarity in pressure-temperature paths the sample follows in these measurements. They both crystallize in the fcc structure and when this work started no phase transitions had been documented experimentally. Very recently, a bcc phase has been reported for Au under shock compression above 200 GPa and also along a ramp-compression path near 400 GPa [13,27,28]. Ta and W form the bcc structure and no phase transitions have been reported in the pressure range accessed here [29–31]. Their pressure-density relationships have also been measured under ramp compression, although only up to ∼300 GPa (at the Omega Laser – University of Rochester, NY – for Ta [32] and at the Z Pulsed Power Facility – Sandia National Laboratories, NM – for W [33]).

Because these materials are dense high-Z metals, they could absorb a large portion of the x-ray spectrum generated by the laser ablation during the ramp compression, leading to heating and thermal expansion of the calibrant itself, resulting in an underestimation of the pressure. To evaluate possible effects due to preheating, we build targets with alternate calibrant placement, so that each calibrant is either on the ablator or on the window side in different experiments, (i.e., Au/Ta and Ta/Au pairs as well as Pt/W and W/Pt, inset of Fig. 1). We would expect any significant preheating to be revealed as a systematically lower density for the layer closer to the ablator due to thermal expansion.

In order to evaluate the fidelity of the *in situ* pressure calibrants, we perform a series of different experiments spanning a pressure range from about 200 to 600 GPa (a range routinely accessed in dynamic compression x-ray diffraction measurements) and compare the pressure values obtained from the methodology relying on the VISAR analysis with the one based on XRD measurements. Finally we demonstrate the new method of pressure determination in ramp-compression x-ray diffraction measurements of an iron sample.

The experiments are performed at the Omega Laser Facility [34]. We use the Powder X-Ray Diffraction Image Plate (PXRDIP) diagnostic [2] to collect diffraction patterns of ramp-compressed Au, Ta, Pt, W, and Fe. A schematic representation of the experimental geometry is shown in Fig. 1. The diagnostic consists of a metallic box containing image plate detectors. The target assembly is placed above a small aperture in the front plate where it is irradiated by 4–6 Omega laser beams with slowly-increasing power and variable total energy to achieve ramp compression to different final pressures [Fig. 2(a), red curve]. The drive laser beams use distributed phase plates, generating an ∼800-μm-diameter supergaussian smooth imprint on the target.

A quasimonochromatic x-ray source is generated by laser-irradiating a Fe, Cu, or Ge foil positioned about 24 mm away from the main target at about 45° with 8–16 additional laser beams defocused to ∼250 μm diameter, without phase plates. These beams are fed with a 1-ns square pulse [Fig. 2(a), blue curve] precisely timed to capture a XRD snapshot at peak compression and their energy is adjusted to optimize the emission of the He-α radiation, generating x-rays at 6.683 keV, 8.368 keV, and 10.249 keV (for Fe, Cu, and Ge, respectively [35]).

This experimental setup allows for simultaneous velocimetry measurements, where the VISAR laser probe (532 nm) can be focused on the rear surface of the target. The line-imaging VISAR system has two interferometers with different velocity sensitivities—or VPF, velocity per fringe—(1.64 and 2.73 km/s/fringe, in these experiments) and is equipped with streak-cameras which record the Doppler-shifted light reflected off the target. While diamond becomes opaque to the VISAR laser once it is compressed above the HEL [illustrated by the strong reduction in fringe intensity at time $t > 2.5$ ns in Fig. 2(b)], the real part of its refractive index remains high so that a significant reflection of the VISAR laser occurs at the diamond/vacuum interface (also referred to as the diamond-free surface), roughly equal to the 17% reflectivity of diamond at ambient conditions. Unfolding the fringe motion after $t \sim 3.8$ ns therefore yields the diamond-free surface velocity [yellow curve, right scale in Fig. 2(b)].

The targets consist of a ∼20 μm diamond ablator and a ∼40 μm diamond window enclosing either two pressure calibrants (a combination of Au/Ta or Pt/W), each one 1-μm thick (left inset of Fig. 1) or a single pressure calibrant (0.5 μm Au or Pt) and a sample (4.5 μm Fe) (right inset of Fig. 1). To minimize the number of glue bonds between the different layers, the pressure calibrants are directly deposited by physical vapor deposition (PVD) onto the diamond window before the ablator is glued onto them. Similarly, Pt or Au are coated onto the iron foil and the stack glued to the diamonds. Glue bonds are determined to be ∼1 μm thick [5]. Thin metal coatings may be characterized by some level of porosity, making the initial density up to a few percent lower than the bulk density. However, recent shock compression and x-ray diffraction experiments using thin Au samples prepared by similar PVD methods have not revealed any noticeable pressure-density anomaly due to unexpected porosity or texture [13]. Each target includes a Ta pinhole (PH) aperture, 300 μm in diameter and 75–150 μm thick, that provides collimation to the divergent x-ray source, as well as a reference diffraction pattern used to determine the position of the image plates relative to the sample and the x-ray source [2,5].
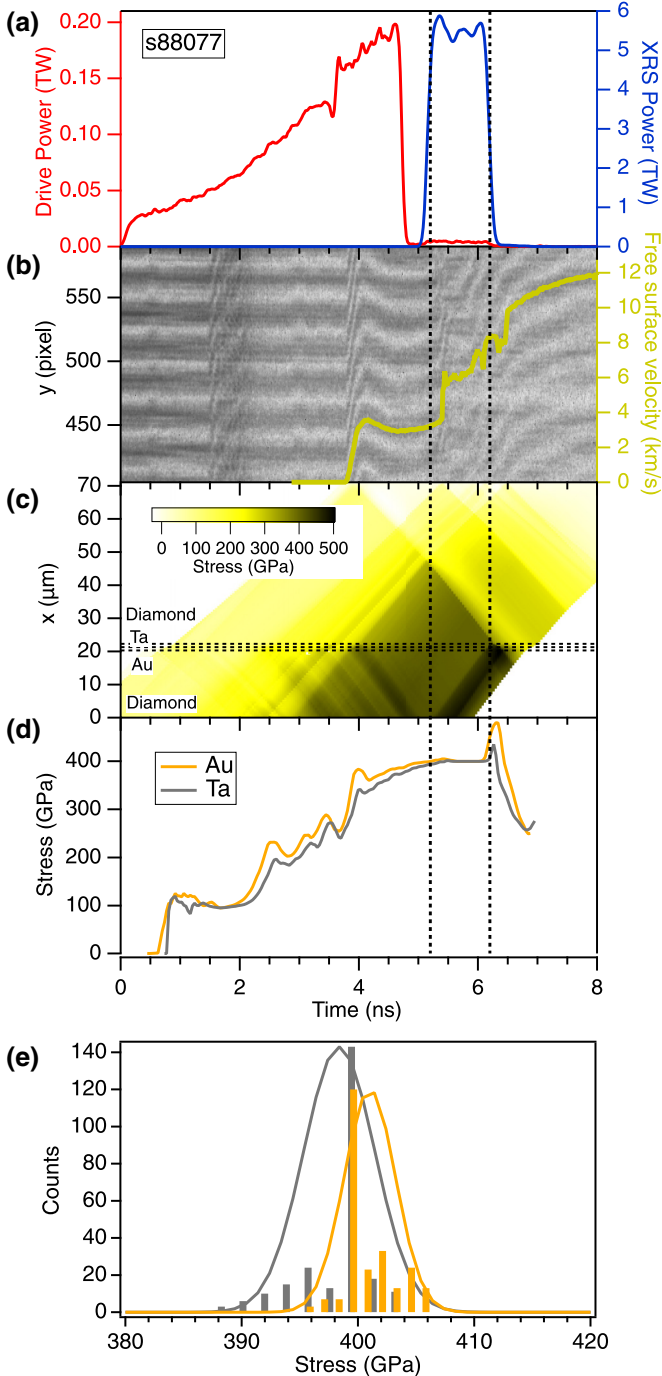
FIG. 2. Example VISAR data and analysis (experiment s88077). (a) Pulse shapes used to compress the Au/Ta samples to about 400 GPa (red) and to generate He-α radiation off a Cu x-ray source (blue). (b) Measured VISAR image (*y* position, left axis—see Fig. 1 for *x-y* coordinates) and extracted diamond free-surface velocity (yellow, right axis), corresponding to the fringe motion recorded after 3.8 ns. Early time motion corresponds to the VISAR probe reflecting off the sample/diamond interface. (c) Inferred pressure map in Lagrangian position *x* as a function of time. Horizontal dashed lines indicate the different layers within the target. (d) Pressure histories of Au (yellow) and Ta (gray) obtained from the characteristics analysis. Vertical-dashed lines indicate the timing of the 1-ns-long x-ray exposure. (e) Distribution of the pressure states within the Au (yellow) and Ta (gray) layers during the x-ray exposure and Gaussian curves representing the mean and standard deviations of the distributions.

IV. VISAR AND X-RAY DIFFRACTION DATA ANALYSIS

Representative VISAR data obtained in experiment s88077 for a Au/Ta sample pair are shown in Fig. 2(b). The yellow curve represents the diamond free-surface velocity, shown on top of the raw VISAR image. We use this measurement as a boundary condition in a characteristics analysis [36,37] to unfold the stress[1] and particle velocity states achieved during the dynamic compression. In this analysis, we backward propagate the measured free-surface velocity to the first material interface. Once the interface conditions as a function of time are determined, we use this calculated interface history to proceed backwards to the next material interface, iterating until we arrive at the laser-ablated surface. We account for the interactions between backward- and forward-propagating waves and rely on previous experiments (for diamond) or theoretical models (for the sample layers) to describe the pressure dependent sound speed and density under ramp compression. Note that this wave characteristics method assumes isentropic behavior during compression and decompression for the various layers. Here we use the tabular EOS Sesame #2700 for Au, Sesame #3520 for Ta, Sesame #3730 for Pt, LEOS #740 for W and Sesame #2150 for Fe, and the measured stress-density and sound speed-particle velocity relationships from ramp-compression experiments [21] for diamond.

It is important to point out that for samples much thinner than the diamond ablator and window (which is the case in these experiments) reverberations will equilibrate the pressure in the sample with the one of the surrounding diamonds. Therefore, if the peak pressure is held sufficiently long, the final pressure state is weakly dependent on the sample EOS. By including it in the analysis, we can however more accurately predict the timing associated with the sample pressure equilibrating to the diamond and therefore optimize the timing of the x-ray probe.

The backwards-characteristics technique allows us to determine the particle velocity and pressure maps in $x - t$ space, where x is Lagrangian longitudinal position and t is time [Fig. 2(c)]. From that we can isolate the stress history within the samples of interest [Au and Ta in Fig. 2(d), represented by the yellow and gray curves, respectively].

Figure 2(d) shows that the pressure in the two layers increases over 6 ns. After about 4.5 ns the two samples have reached pressure equilibrium and during the x-ray probe time (dashed-vertical lines in Fig. 2), their pressure differs by less than 10 GPa, as a result of the fast wave reverberations within the two thin samples. Final stresses are obtained from the average and standard deviation of the stress distribution during the x-ray exposure, shown in Fig. 2(e) together with the corresponding Gaussian curves. While Fig. 2(d) highlights the time uniformity of the pressure in the samples, Fig. 2(e) shows that during the x-ray exposure the pressure is also spatially uniform. The distribution of the pressure states in each sample is within 10 GPa (as shown by the width of the Gaussian

---

[1]In the experiments described here, VISAR documents the longitudinal velocity, which we use to infer the longitudinal stress (P_x). To simplify the notation, in this paper we will use the terms stress and pressure interchangeably.

TABLE I. Pressure and uncertainty obtained from analysis of the VISAR data (P_{VISAR}) for the two layers (L1 towards the ablator and L2 towards the window), as well as pressure obtained from the diffraction pattern and the calibrant P_x-ρ EOS (P_{XRD}). The blank fields correspond to experiments where no diffraction signal from the calibrant is observed.

Exp ID	Target L1/L2	P_{VISAR} L1 (GPa)			P_{VISAR} L2 (GPa)			P_{XRD} (GPa)		P_{XRD} (GPa)	
		P_{L1}	ΔP^-	ΔP^+	P_{L2}	ΔP^-	ΔP^+	P_{fcc}	ΔP_{fcc}	P_{bcc}	ΔP_{bcc}
83490	Au/Ta	180	16	53	167	13	52	215	5	198	5
88077	Au/Ta	401	15	52	398	15	52	416	18	365	7
91873	Au/Ta	491	40	64	454	42	66	524	19		
83493	Ta/Au	253	81	96	200	64	82	183	4	182	19
94402	Ta/Au	375	45	67	354	41	65			333	8
91881	Ta/Au	449	19	53	442	17	53	392	12		
83492	Pt/W	185	61	79	143	42	65	189	7	149	4
88081	Pt/W	380	15	52	378	14	52	387	13	371	6
83494	W/Pt	252	23	55	223	26	57	194	6		
88080	W/Pt	385	16	53	382	14	52	344	12		
94403	W/Pt	613	54	73	574	43	66	560	18		
79541	Au/Fe	229	9	51	227	9	51	230	4	N/A	
81488	Fe/Pt	246	11	51	236	12	51	264	6	N/A	

curves) and the pressures of the two samples agree to within 3 GPa (as shown by the centroids of the distributions).

The uncertainty in the pressure determination using this method originates from various sources. The uncertainty in the velocity measurement with VISAR (up to 5% of the VPF) contributes to about 1–2% error in pressure. Pressure gradients within the sample and errors related to the uncertainty in the thickness of each target component (including glue bonds) have a variable contribution ranging from 2% to 8% of the total pressure uncertainty. The importance of this contribution to the total error budget depends on how close in time to peak compression the x-rays are generated, how steady the final pressure state is, as well as how accurately the thickness of the various target components is known. An additional 3% is related to the uncertainty in the diamond compressibility under ramp compression [21]. The total error from these sources (obtained by adding in quadrature these uncorrelated contributions) usually amounts to less than 20 GPa, although it can be larger in the presence of pressure gradients. The largest contribution to the total uncertainty is related to the assumption that diamond follows a reversible isentropic path upon compression and release, which is made within the characteristics analysis framework. This leads to a possible underestimate of the stress of about 50 GPa, which we represent with an asymmetric error bar [38] (Table I).

For experiment s88077, which we illustrate here as an example, the final pressure and uncertainty are $P_{Au} = 401(+52/-15)$ GPa and $P_{Ta} = 398(+52/-15)$ GPa (see Table I for other experiments).

Representative x-ray diffraction data are shown in Figs. 3, 5, and 7. The data are projected into the $\phi-2\theta$ space, ϕ being the azimuthal angle around the direction of the direct x-ray beam and 2θ the Bragg angle corresponding to scattering originating at the sample location. The projection takes into account the corrections to the diffraction angle described in Ref. [5]. Masked regions (white patches) correspond to signal due either to diffraction from the single crystal diamonds or to fluorescence from the metallic components of the diagnostic box, that are excluded from the lineout.

The azimuthally-averaged one-dimensional lineouts are shown in black below the corresponding two-dimensional data. The Bragg peaks are fit to Gaussian profiles to determine the 2θ positions of the different reflections from which the d spacings can be calculated. The uncertainty in the Bragg peak positions accounts for the error associated with the Gaussian fit, as well as for the goodness of the reconstruction of the scattering geometry, evaluated from the deviation of the reference pinhole lines from their expected 2θ position. The total uncertainty on 2θ is on the order of 0.1%, resulting in 0.2% uncertainty on the d spacing. From the measured d spacings and if the crystal structure is known, one can obtain the lattice parameter and therefore the density of the samples at the pressure during the x-ray exposure (i.e., peak pressure if the diffraction experiment is timed correctly). Typical uncertainties in the density are on the order of 0.6% (Tables II and III).

In order to evaluate the pressure from the calibrant we use (when possible) equations of state measured in dedicated ramp-compression experiments to keep the compression path similar to the one followed in our experiments, therefore minimizing thermal effects. The Au and Pt P_x-ρ EOS used here are from ramp-compression experiments up to TPa pressure [26] at the National Ignition Facility (NIF). For Ta we use the pressure-density relationship from similar experiments at the Omega Laser Facility [32] up to about 300 GPa and extrapolated to ~600 GPa (the maximum pressure reached in our measurements) using a Vinet fit. In the absence of high fidelity EOS for W under ramp compression (see Sec. V B for further discussion), we use the 300 K isotherm measured in diamond anvil cell experiments [17] up to 150 GPa and extrapolated to higher pressure.

The uncertainty in the final pressure determination accounts for the uncertainty in the measured P_x-ρ relationship for the standard material as well as the uncertainty on the density of the sample from x-ray diffraction. For each density value ($\rho \pm \Delta\rho$, where $\Delta\rho$ is the uncertainty on the density) we use a Monte Carlo approach to vary the density within its uncertainty and calculate a distribution of corresponding pressures based on the calibrant EOS. The average of these

TABLE II. Measured *d*-spacings and calculated lattice parameters and densities for the experiments that used the Au, Ta, Pt, and W calibrants.

Exp ID	Target	*fcc* structure						*bcc* structure				
		d_{111} (Å)	d_{200} (Å)	d_{220} (Å)	d_{113} (Å)	a (Å)	ρ (g/cm³)	d_{110} (Å)	d_{200} (Å)	d_{112} (Å)	a (Å)	ρ (g/cm³)
83490	Au/Ta		1.789(3)	1.253(3)		3.567(5)	28.8(1)			1.162(2)	2.846(5)	26.1(1)
88077	Au/Ta	1.965(6)				3.40(1)	33.2(3)	1.908(3)		1.095(2)	2.691(3)	30.8(1)
91873	Au/Ta	1.929(5)				3.341(9)	35.1(3)					
83493	Ta/Au	2.065(4)	1.803(4)	1.271(2)	1.097(2)	3.603(3)	27.96(8)			1.17(1)	2.86(2)	25.5(6)
94402	Ta/Au							1.920(3)			2.715(4)	30.0(1)
91881	Ta/Au	1.974(4)				3.419(7)	32.7(2)					
83492	Pt/W	2.036(5)	1.775(5)	1.256(3)	1.078(5)	3.545(5)	29.1(1)	2.036(5)	1.438(8)	1.169(3)	2.872(5)	25.8(1)
88081	Pt/W	1.958(4)				3.391(5)	33.2(2)	1.896(3)		1.090(3)	2.678(4)	31.8(1)
83494	W/Pt	2.030(5)	1.766(4)	1.256(3)	1.076(3)	3.540(4)	29.2(1)					
88080	W/Pt	1.975(4)	1.722(6)	1.198(4)		3.418(5)	32.4(2)					
94403	W/Pt	1.905(5)	1.656(4)	1.166(3)	0.995(3)	3.303(4)	36.0(1)					

pressure values and the standard deviation of the distribution provide us with the inferred pressure from the calibrant and its uncertainty. Systematic uncertainties due to the use of different EOS for the calibrants are not included.

For experiment s88077 we obtain $P_{Au} = 416 \pm 18$ GPa and $P_{Ta} = 365 \pm 7$ GPa from the experimentally derived densities and the equations of state for Au and Ta [26,32], in very good agreement with the pressure determination from the VISAR data and characteristics analysis (see Table I for other experiments).

V. RESULTS

A. Au and Ta pressure calibrants

Figure 3 shows the results from experiments s88077 and s94402 that aimed at reaching the same pressure (about 400 GPa) with opposite coating positions (Au/Ta on the top panel and Ta/Au on the bottom panel).

The diffraction data for experiment s88077 [Fig. 3(a)] show a broad peak near $2\theta \sim 45°$ that is assigned to the Au(111) and Ta(110) reflections that are very closely located at this pressure and almost merge into a single peak. While the structural assignment for Ta is unambiguous because of the observation of the Ta(112) reflection, confirming the bcc lattice, Au only shows one main peak in this particular experiment (up to four diffraction peaks consistent with the fcc lattice have been observed in different experiments, see Table II). Based on density arguments we can assign the observed peak to the fcc (111) reflection. A phase transition to the bcc structure has been reported for ramp-compressed Au near 400 GPa [28]. Interpreting the diffraction peak as the (110) line of bcc-Au would result in a density of about

22 g/cm³ which is too low given the pressure reached in this experiment. All the experiments that use a Au layer obtained in this study are consistent with the fcc structure.

Figure 3(b) shows the data for the companion experiment with Ta/Au coatings. In this case no diffraction peaks from the gold sample are observed. The 2θ position of the Ta(110) peak is close to the one obtained in experiment s88077, as expected for similar final pressures. In both experiments peak overlap between the Ta pinhole (asterisks) and the samples (yellow and gray tick marks and Miller index labels) complicates the identification of additional diffraction lines from the compressed samples.

The absence of Au diffraction peaks cannot be interpreted as a result of alloying. Although gold and tantalum can form an alloy [39], the tetragonal structure that has been reported does not match the experimentally observed diffraction pattern. The tetragonal distortion of the bcc lattice results in splitting of the main bcc diffraction peaks and the data shown in Fig. 3(b) are not consistent with this. Additionally, even assuming that the high temperatures associated with the dynamic compression, could induce sufficiently fast (nanosecond) atomic diffusion, it would still be hard to explain why this would happen only in one experiment (considering that the other diffraction patterns show either peaks from Au and Ta or an fcc lattice that can be explained by pure Au). We interpret the absence of Au peaks in experiment s94402 as due to issues with the Au coating in that particular target.

The stress-density data obtained in the measurements for Au and Ta are shown in Fig. 4. The data are presented as they would in a typical diffraction experiment under dynamic compression, i.e., stress (P_x) obtained from the VISAR analysis as a function of the density obtained from the diffraction (see

TABLE III. Measured *d* spacings and calculated lattice parameters and densities for the diffraction experiments on ramp-compressed iron that used a Au or Pt pressure calibrant.

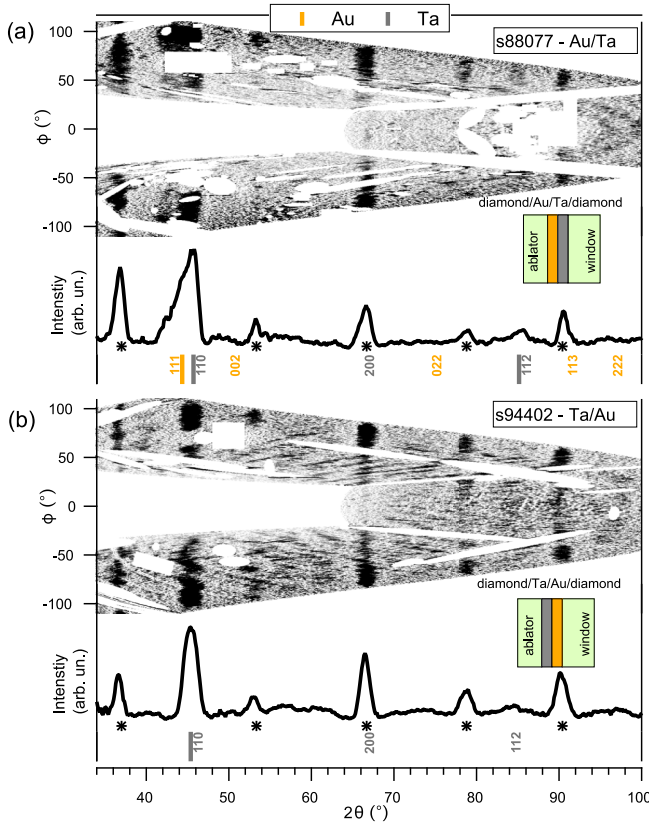| Exp ID	Target	*fcc* structure					*hcp* structure							
		d_{111}(Å)	d_{200}(Å)	d_{220}(Å)	a (Å)	ρ (g/cm³)	d_{100}(Å)	d_{002}(Å)	d_{101}(Å)	d_{102}(Å)	a (Å)	c (Å)	c/a	ρ (g/cm³)
79541	Au/Fe	2.051(2)	1.770(5)		3.551(3)	29.22(8)	1.884(2)	1.770(5)	1.678(3)		2.183(2)	3.515(3)	1.61	12.78(2)
81488	Fe/Pt	2.006(1)	1.742(1)	1.226(1)	3.477(1)	30.84(3)	1.862(2)	1.742(1)	1.645(5)	1.280(1)	2.164(1)	3.483(1)	1.61	13.13(1)

FIG. 3. X-ray diffraction patterns for experiments s88077 [Au/Ta pair, panel (a)] and s94402 [Ta/Au pair, panel (b)] for ramp compression to about 400 GPa. The images show the projection of the diffraction data in ϕ (azimuthal angle) vs 2θ (sample Bragg angle [5]) space. The black curves represent the one-dimensional lineout and vertical tick marks identify the peaks originating from compressed Au (yellow) or Ta (gray) used to calculate the density. The expected position of the other reflections either not observed or overlapping with the Ta pinhole for the fcc and bcc structures are indicated by the corresponding Miller indices. Peaks originating from the Ta collimating pinhole at ambient density are highlighted by asterisks. No peaks for Au are observed in s94402. The x-ray source is Cu He-α radiation at 8.368 keV [35].

FIG. 4. Results of the experiments on ramp-compressed Au and Ta pairs. The data are shown as stress from VISAR (P_x^{VISAR}) as a function of density from diffraction (ρ_{XRD}). Different symbols are used to identify different experiments (square: s83490; up-pointing triangle: s88077; diamond: s91873; circle: s83493; down-pointing triangle: s94402 and left-pointing triangle: s91881). Colors are used to indicate data for Au (yellow) and Ta (gray) samples. Full symbols identify the pressure-density values for the material closer to the ablator, while empty symbols correspond to the material coated on the window. Our data are compared with experimental pressure-density relationships for Au (yellow curve) [26] and Ta (gray curve) [32], the latter extrapolated above ~320 GPa (dashed-gray line). The bottom panel shows the percentage difference between the stress obtained from VISAR and the value obtained from the samples diffraction pattern and their EOS. The shaded area highlights that the two pressure determination methods agree to within 20% for the majority of the experiments.

figure caption for symbols). They are compared with their respective P_x-ρ equations of state from ramp-compression experiments [26,32] (Au in yellow and Ta in gray). As shown in the residual plot (bottom panel of Fig. 4) the difference between the stress obtained from VISAR analysis and the value that would be obtained if using Au and Ta as *in situ* pressure calibrants (i.e., using the measured density from diffraction and their known EOS) agree to within 10–20% for the majority of the data (shaded region).

B. Pt and W pressure calibrants

Figure 5 shows representative diffraction data for the experiments using platinum and tungsten as pressure calibrants [s83492 for Pt/W in (a) and s83494 for W/Pt in (b)]. These two experiments aimed at a similar pressure near 200 GPa. The most intense peaks for fcc platinum and bcc tungsten [Pt(111) and W(110)] overlap at this pressure. Nonetheless,
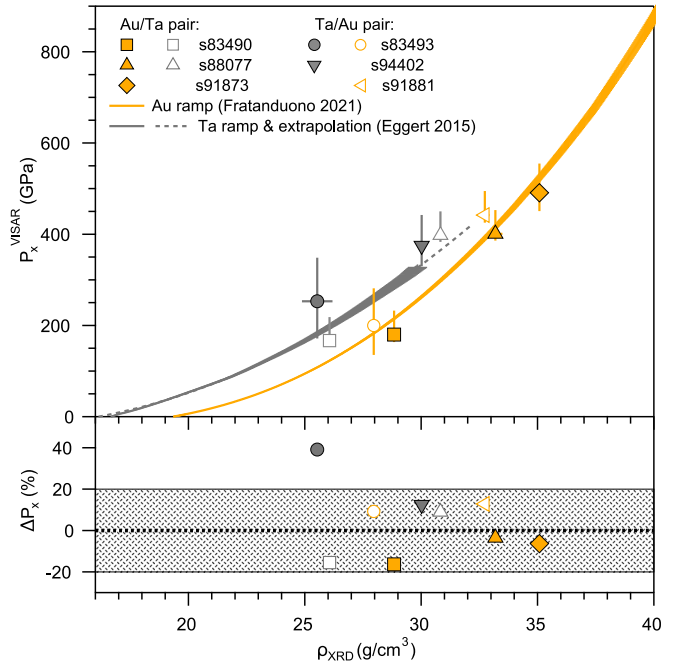
the observation of three additional reflections for Pt [(200), (220), and (113), red tick marks] and of the W(200) peak (blue tick mark, only seen in s83492) confirms the structural assignment. In experiment s83494, as well as in the other two that used the W/Pt coating pair, only reflections for Pt are unambiguously identified (see Table II).

The possibility of formation of a Pt-W alloy has been explored to explain the absence of diffraction signal from bcc-W in these experiments. Pt and W have been reported to form an alloy with an fcc structure [40], which could be consistent with the diffraction patterns observed in the experiments using W/Pt pairs. However, for that to be possible, the timescale for atomic diffusion would have to be faster than ~4 ns (the timescale of the compression in our experiments). For a typical solid atomic diffusion of about 10^{-10} m^2/s [41] it would take about 50 μs for a particle to diffuse through 100 nm. Additionally, in the absence of a reasonable mechanism explaining alloying only in those experiments using targets with the W coated on the Pt and not the other way around, we tend
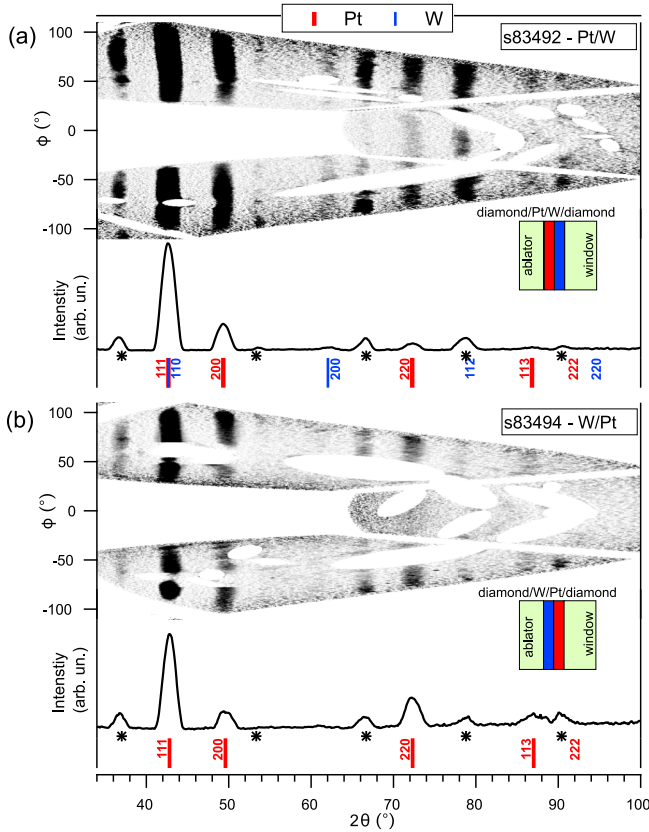
FIG. 5. X-ray diffraction data for experiment s83492 (a) and s83494 (b) for ∼200 GPa ramp compression in Pt and W samples. The top panel shows the data for the Pt/W pair and the bottom panel for the W/Pt one. Diffraction data are projected into ϕ (azimuthal angle) vs 2θ (sample Bragg angle [5]) space. Black curves represent the one-dimensional lineouts and peaks are identified as due to the Ta pinhole (asterisks), the compressed fcc-Pt (red tick marks) and the compressed bcc-W (blue tick marks). Other reflections for these structures not used to determine the density because of peak overlap are indicated by their Miller indices. No peaks for W are observed in experiment s83494. X-ray energy is 8.368 keV from Cu He-α radiation [35].

to exclude this explanation. Therefore, although we cannot conclusively rule out the possibility of alloying between Pt and W, we believe that the most likely interpretation is an issue related to the W coating when changing the substrate from diamond to Pt.

Figure 6 compares the stress (from VISAR) and density (from diffraction) obtained in our experiments with P_x-ρ curves from literature. Red and blue colors correspond to Pt and W, respectively. Our data on Pt (see figure caption for details) are in very good agreement with the stress-density EOS measured in ramp-compression experiments (red line) [26]. The pressure-density data for W (blue symbols) are compared with different EOS models: a 300-K isotherm from measurements with diamond anvil cells (solid blue line and dashed-dot-dot line for its extrapolation) [17], data from ramp-compression experiments on the Z facility (dash-dot line and dotted line for extrapolation) [33], an isentrope from tabular EOS LEOS #740 (dashed line) and Hugoniot data (blue plus signs) [42]. Our data are consistent with the isotherm
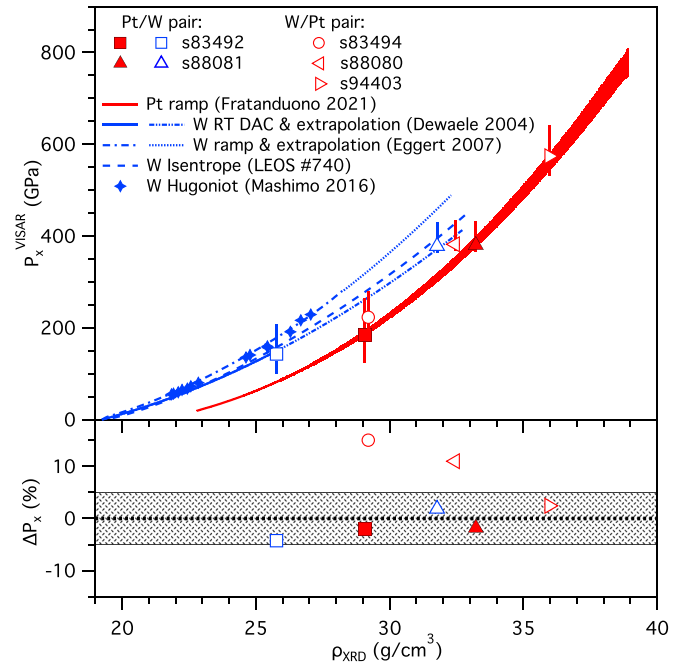

FIG. 6. Results of the experiments using Pt and W as pressure standards. The data show stress from VISAR (P_x^{VISAR}) as a function of density from diffraction (ρ_{XRD}). Different symbols identify different experiments (square: s83492; up-pointing triangle: s88081; circle: s83494; left-pointing triangle: s88080; and right-pointing triangle: 94403), colors correspond to the material (Pt in red and W in blue) and full/empty symbols locate the material within the target (towards the ablator/window, respectively). The data are compared with P_x-ρ relationships from ramp-compression experiments for Pt (red-solid line [26]) and different EOS models for W: the room-temperature (RT) cold curve from DAC experiments [17] (blue-solid line) extrapolated to 400 GPa (dash-dot-dot line); the isentrope calculated from LEOS #740 (dashed-blue line); ramp-compression data [33] up to 300 GPa (dash-dotted line) and extrapolation (dotted line); shock-compression (Hugoniot) data [42] (blue-plus signs). The bottom panel shows the percentage difference between the stress obtained from the VISAR analysis and the one obtained using the observed diffraction peaks and the Pt or W EOS [17,26]. For the majority of the experiments the pressure determined from the two methods agree to within 5%.

and the isentrope curves and not with the pressure-density relationship from ramp-compression experiments (at least at 400 GPa). It is important to point out that this dataset may be affected by experimental issues related to drive nonuniformity [33], which could explain why they overlap with data from shock-compression experiments (blue plus signs) despite the expected lower thermal pressure associated with ramp compression. We therefore utilize the DAC data [17] in our analysis, which we extrapolate to ∼400 GPa (blue dashed-dot-dot line). Using the tabular EOS LEOS #740 we estimate the error in using the cold curve to be about 20 GPa which is the maximum difference in pressure between the cold curve and the principle isentrope (dashed-blue line) at the same density in the pressure range explored in this study.

The residual plot shows the difference in the pressure determined from the VISAR analysis and from the reference
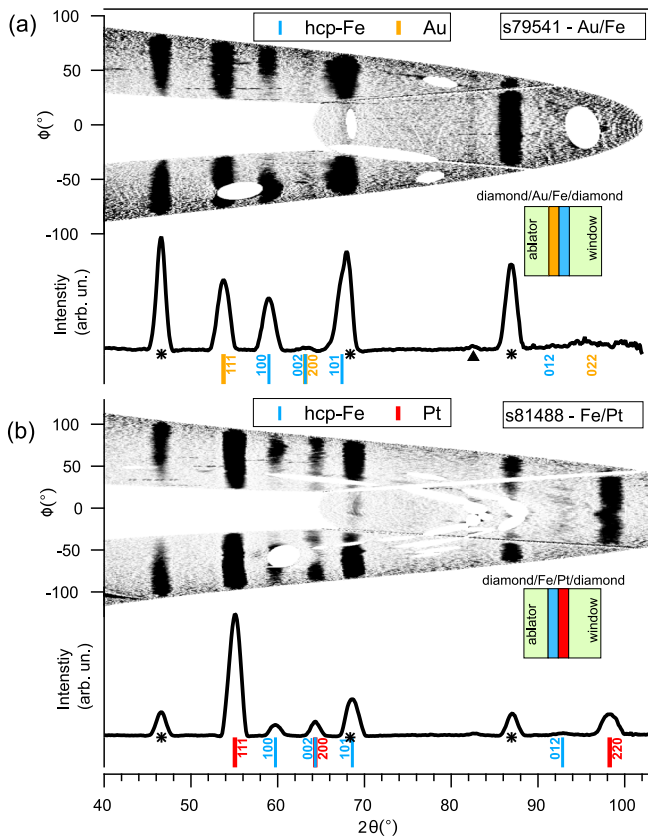
FIG. 7. Diffraction patterns obtained for ramp-compression experiments of iron to about 250 GPa, using Au (a) or Pt (b) pressure calibrants. Data are projected into ϕ (azimuthal angle)–2θ (sample Bragg angle [5]) space. Black curves are the one-dimensional lineouts. Peaks are associated with either fcc-Au (yellow), fcc-Pt (red), hcp-Fe (cyan), or Ta pinhole (asterisk and triangle for secondary Ly-α emission, see text).

EOS, measured under ramp compression for Pt and in DAC experiments for W. For the vast majority of the experiments, the pressure determined from VISAR agrees within 5% of the value obtained from the standard EOS and the points showing the largest deviation remain within the 10–15% range.

C. X-ray diffraction of ramp-compressed iron

To illustrate the validity of this approach as an alternative method for pressure determination in x-ray diffraction dynamic-compression experiments we collect diffraction patterns of ramp-compressed iron, where the target assembly includes a 0.5 μm Pt or Au pressure standard (Fig. 1, right inset). The diffraction data obtained using an iron x-ray source (E = 6.683 keV) are shown in Fig. 7 and peaks are assigned to compressed hcp-Fe (cyan) and fcc-Au (yellow, s79541) or fcc-Pt (red, s81488), in addition to ambient density Ta originating from the pinhole aperture (asterisks). Contributions from the Ly-α secondary emission (triangle), which is strong enough for an iron x-ray source to generate a measurable diffraction signal [35], are also visible. Up to four diffraction peaks are used to get the density of iron (see Table III), fixing the c/a for the hcp structure to 1.61 (Supplemental Material for Ref. [43]).
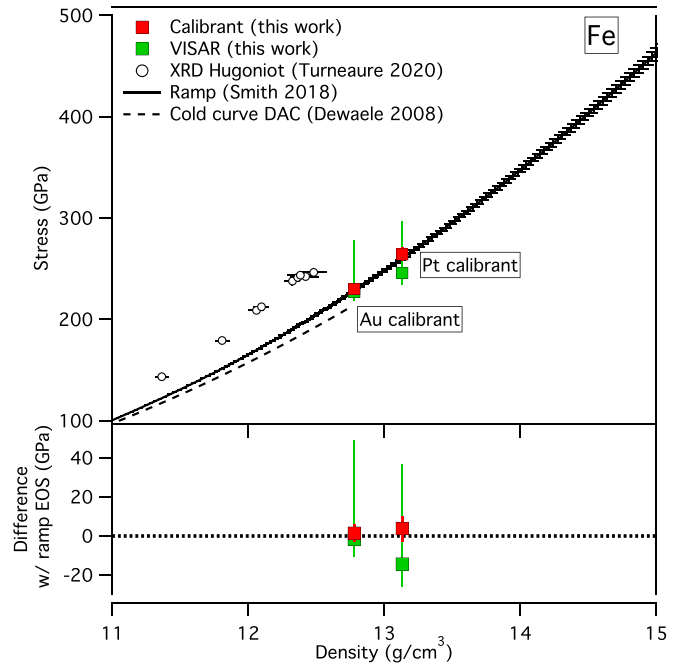

FIG. 8. Stress-density models for iron (ramp compression [20], cold curve from DAC XRD [17] and Hugoniot data from x-ray diffraction under shock compression [46]) compared with the results of our x-ray diffraction experiments under ramp compression, where pressure is obtained from either VISAR analysis (green squares) or from the XRD pattern and the EOS of Au or Pt calibrants (red squares). The bottom panel shows the difference between the pressure determinations in our experiments with the P_x-ρ relationship from ramp-compression experiments [44].

According to the VISAR data and analysis, the iron is compressed to P_{VISAR} = 227 (+51/–9) GPa and P_{VISAR} = 246 (+51/–11) GPa in experiments s79541 and s81488, respectively. The characteristics analysis shows good pressure equilibrium between the Fe sample and the calibrant, as can be inferred from the pressure difference between the two layers, which is only 2 GPa and 10 GPa in the two experiments (Table I). Using the measured lattice parameter for Au and Pt and the EOS measured in ramp-compression experiments [26] we obtain P_{XRD} = 230 ($\pm$4) GPa and P_{XRD} = 264 ($\pm$ 6) GPa, which are very close to the values obtained from the VISAR data.

Figure 8 shows the stress of the iron sample obtained in these experiments using the two methods (green and red squares for values obtained from VISAR and XRD, respectively) as a function of the iron density obtained from diffraction. Our data are compared with different stress-density curves, including a P_x-ρ curve measured in ramp-compression experiments [44] (solid line), a 300-K isotherm from static-compression diffraction [45] (dashed line) and results from diffraction experiments under shock compression (Hugoniot) [46] (empty circles). Our pressure-density data for hcp-Fe agree very well with the EOS model from ramp-compression experiments [44]. To illustrate this, we calculate the difference between the four pressure determinations and the ramp P_x-ρ relationship (at the experimentally determined density) and show the result in the bottom panel
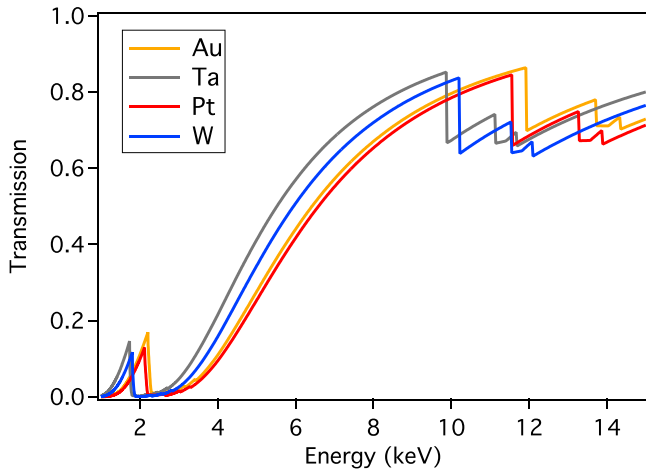
FIG. 9. Calculated x-ray transmission curves for 1-μm-thick Au (yellow), Ta (gray), Pt (red), and W (blue) in the 1–15 keV range, showing that most of the x-rays below 6 keV are absorbed by these metals.
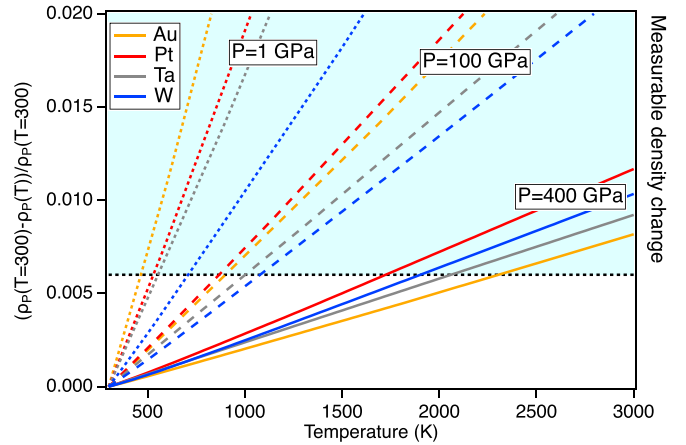

FIG. 10. Relative density change due to thermal expansion for Au (yellow), Pt (red), Ta (gray), and W (blue) at 1 GPa (dotted line), 100 GPa (dashed lines), and 400 GPa (solid lines) calculated using thermal equations of state available in literature (Ref. [26] for Au and Pt, Ref. [48] for Ta, and Ref. [49] for W). The precision of the density determination in our x-ray diffraction measurements is ~0.6%, therefore we expect to be able to measure density changes represented by the cyan-background area.

of Fig. 8. All the measurements agree to better than 20 GPa with the ramp data. Remarkably the uncertainty in pressures determined from the use of *in situ* pressure calibrants is significantly smaller (about a factor of four) than the uncertainty associated with the determination from VISAR measurements and the characteristics analysis.

VI. DISCUSSION

A. No evidence for sample preheating from ablation plasma

In our experiments we achieve ramp compression by laser ablation of diamond. This generates a continuous x-ray radiation that propagates through the target and is in part absorbed by the different layers. As shown in Fig. 9, for the sample materials used in this paper, x-ray transmission exceeds 50% only above ~6 keV, implying that lower energy x-rays will be mostly absorbed, potentially preheating the sample. Understanding the level of preheating is critical to correctly interpret the results of laser-driven dynamic compression experiments, as phase transitions can be driven by temperature in addition to pressure. Moreover, when using *in situ* pressure calibrants, if preheating is substantial, thermal expansion of the lattice has to be taken into account in the density determination in order to avoid a systematic pressure underestimate.

In this paper, the density determination has an average relative uncertainty of $\Delta\rho/\rho \sim 0.6\%$ (black-dashed line in Fig. 10). Using thermal equations of state for Au, Pt, Ta, and W available in the literature (see caption of Fig. 10) we can calculate the expected density change due to thermal expansion at different pressures (1 GPa, 100 GPa, and 400 GPa, Fig. 10). As expected, the higher the pressure, the higher the temperature increase needed to generate a given density change. We can see that already for a compression to a moderate pressure of 400 GPa a temperature of at least 1800–2500 K (depending on the material) is required to produce a lattice expansion discernible with our experimental setup (cyan-shaded background in Fig. 10). Our data collected on pairs of the same samples with alternate position within the

target assembly do not show any systematic density decrease when the layer is towards the ablator (and therefore expected to absorb the majority of the x-rays produced by the ablation). We therefore conclude that in the pressure range explored in this study, either there is no significant heating due to ablation plasma or the temperature generated does not exceed ~2000 K.

The fact that we do not conclusively observe a diffraction signal from W when it is coated towards the ablator, is hardly associated with preheating-induced melting, as W has the highest melting temperature at ambient pressure among the metals studied here. A more likely explanation could be related to issues with the coating itself when changing the substrate from diamond to Pt.

If preheating does not affect the measured density in a significant way, then the method based on pressure calibrants can be used to both validate the pressure determination from VISAR analysis, as well as an alternate, more precise way of measuring pressure in ramp-compression x-ray diffraction experiments.

This study shows that the pressures determined from diamond free-surface velocity measurements and the characteristic analysis are consistent with the one obtained using *in situ* pressure calibrants. Figure 11 shows the stress obtained from the VISAR analysis as a function of the stress obtained from the XRD pattern of the calibrants and their pressure-density EOS (top panel), as well as their difference (bottom panel). For the majority of the experiments the two methods agree to within ~40 GPa (shaded region), validating a method for pressure determination that is frequently used in diffraction experiments at the Omega Laser Facility [10,12,14,15,28,47] and on the NIF [9].

The use of *in situ* pressure calibrants also allows us to determine pressure with about a factor of four higher precision than
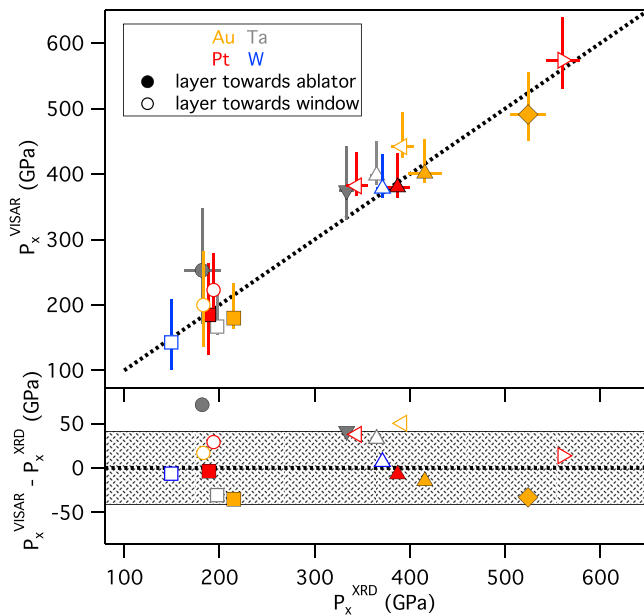
FIG. 11. Stress obtained from the VISAR analysis as a function of stress obtained from the diffraction data and the material EOS. Symbols and colors follow the same convention as in Figs. 4 and 6. As can be observed in the residual plot on the bottom panel, in the majority of our experiments the two methods agree to within ∼40 GPa.

relying only on diamond free-surface velocity measurements (Table I).

B. Recommended pressure calibrants

Among the metals investigated here, Pt appears to be the most reliable pressure calibrant, providing a very strong diffraction signal, with up to four Bragg reflections measured. Strong XRD lines are observed in all the experiments regardless of the coating substrate and the Pt pressure-density EOS upon ramp compression has been measured with high precision up to TPa regime [26], allowing its use in a wide pressure range without extrapolation. Au and Ta also yield good diffraction signal, however in some experiments we could only observe diffraction from one of the two layers. The use of tungsten as pressure calibrant is not recommended, given the possible issues with coating substrates discussed earlier, as well as the absence of a good reference pressure-density relationship.

Ultimately, the calibrant material should be chosen based on the expected diffraction pattern for the sample material and in such a way as to avoid peak overlap as much as possible. To this aim, if using an *in situ* pressure calibrant, it is recommended to avoid having a pinhole material contributing to the diffraction signal, for example using a low-symmetry crystal such as U-6wt% Nb alloy (which does not produce a measurable diffraction pattern) or an amorphous material [5].

VII. CONCLUSIONS

We present the detailed analysis of a series of laser-driven ramp-compression experiments on Au, Ta, Pt, W, and Fe, coupling velocimetry and nanosecond x-ray diffraction measurements. Simultaneous compression of multiple materials enables us to obtain atomic structure information for pairs of different metals on each XRD pattern. These measurements demonstrate that the use of *in situ* pressure calibrants for stress determination in x-ray diffraction dynamic-compression experiments is a viable alternative to VISAR measurements of the diamond free-surface velocity. This has a number of advantages, as there are situations where the VISAR diagnostic may not be available, the VISAR signal may be lost because of melting or blanking of the window, or experimental constraints dictate the use of a window different than diamond and possibly whose EOS is not well characterized.

This paper also validates the currently used method for pressure determination, confirming that VISAR measurements of the diamond free-surface velocity and the method of characteristics (employed to convert velocity into stress) is reliable and in agreement with the pressure obtained from the use of calibrants.

Additionally, this study also provides an important piece of information regarding laser-ablation preheating of the sample, which seems to be nonexistent or negligible in the pressure range explored in this paper.

Enabling a more precise pressure determination, this approach is expected to have important consequences for a variety of fields from high-pressure condensed matter and material science, to geophysics and planetary science.

[1] D. H. Kalantar, E. Bringa, M. Caturla, J. Colvin, K. T. Lorenz, M. Kumar, J. Stolken, M. A. Allen, K. Rosolankova, J. Wark *et al.*, Multiple film plane diagnostic for shocked lattice measurements (invited), Rev. Sci. Instrum. **74**, 1929 (2003).

[2] J. R. Rygg, J. H. Eggert, A. E. Lazicki, F. Coppari, J. A. Hawreliak, D. G. Hicks, R. F. Smith, C. M. Sorce, T. M. Uphaus, B. Yaakobi, and G. W. Collins, Powder diffraction from solids in the terapascal regime. Rev. Sci. Instrum. **83**, 113904 (2012).

[3] J. M. Foster, A. J. Comley, G. S. Case, P. Avraam, S. D. Rothman, A. Higginbotham, E. K. Floyd, E. T. Gumbrell, J. J. Luis, D. McGonegle *et al.*, X-ray diffraction measurements

of plasticity in shock-compressed vanadium in the region of 10-70 GPa, J. Appl. Phys. **122**, 025117 (2017).

[4] A. Denoeud, J. A. Hernandez, T. Vinci, A. Benuzzi-Mounaix, S. Brygoo, A. Berlioux, F. Lefevre, A. Sollier, L. Videau, A. Ravasio *et al.*, X-ray powder diffraction in reflection geometry on multi-beam kJ-type laser facilities, Rev. Sci. Instrum. **92**, 013902 (2021).

[5] J. R. Rygg, R. F. Smith, A. E. Lazicki, D. G. Braun, D. E. Fratanduono, R. G. Kraus, J. M. McNaney, D. C. Swift, C. E. Wehrenberg, F. Coppari *et al.*, X-ray diffraction at the National Ignition Facility, Rev. Sci. Instrum. **91**, 043902 (2020).

[6] D. Broege, S. Fochs, G. Brent, J. Bromage, C. Dorrer, R. F. Earley, M. J. Guardalben, J. A. Marozas, R. G. Roides, J. Sethian *et al.*, The Dynamic Compression Sector laser: A 100-J UV laser for dynamic compression research, Rev. Sci. Instrum. **90**, 053001 (2019).

[7] K. Tono, T. Togashi, Y. Inubushi, T. Sato, T. Katayama, K. Ogawa, H. Ohashi, H. Kimura, S. Takahashi, K. Takeshita *et al.*, Beamline, experimental stations and photon beam diagnostics for the hard x-ray free electron laser of SACLA, New J. Phys. **15**, 083035 (2013).

[8] B. Nagler, B. Arnold, G. Bouchard, R. F. Boyce, R. M. Boyce, A. Callen, M. Campell, R. Curiel, E. Galtier, J. Garofoli *et al.*, The matter in extreme conditions instrument at the Linac Coherent Light Source, J. Synchrotron Radiat. **22**, 520 (2015).

[9] A. Lazicki, D. McGonegle, J. R. Rygg, D. G. Braun, D. C. Swift, G. M. Gorman, R. F. Smith, P. G. Heighway, A. Higginbotham, M. J. Suggit *et al.*, Metastability of diamond ramp-compressed to 2 TPa, Nature (London) **589**, 532 (2021).

[10] F. Coppari, R. F. Smith, J. H. Eggert, J. Wang, J. R. Rygg, A. Lazicki, J. A. Hawreliak, G. W. Collins, and T. S. Duffy, Experimental evidence for a phase transition in magnesium oxide at exoplanet pressures, Nat. Geosci. **6**, 926 (2013).

[11] F. Coppari, R. F. Smith, J. Wang, M. Millot, D. Kim, J. R. Rygg, S. Hamel, J. H. Eggert, and T. S. Duffy, Implications of the iron oxide phase transition on the interiors of rocky exoplanets, Nat. Geosci. **14**, 121 (2021).

[12] A. Lazicki, J. R. Rygg, F. Coppari, D. Fratanduono, R. G. Kraus, G. W. Collins, R. Briggs, D. G. Braun, D. C. Swift, and J. H. Eggert, X-Ray Diffraction of Solid Tin to 1.2 TPa, Phys. Rev. Lett. **115**, 075502 (2015).

[13] R. Briggs, F. Coppari, M. G. Gorman, R. F. Smith, S. J. Tracy, A. L. Coleman, A. Fernandez-Pañella, M. Millot, J. H. Eggert, and D. E. Fratanduono, Measurement of Body-Centered Cubic Gold and Melting under Shock Compression, Phys. Rev. Lett. **123**, 045701 (2019).

[14] M. Millot, F. Coppari, J. R. Rygg, A. Correa Barrios, S. Hamel, D. C. Swift, and J. H. Eggert, Nanosecond X-ray diffraction of shock-compressed superionic water ice, Nature (London) **569**, 251 (2019).

[15] D. E. Fratanduono, R. F. Smith, S. J. Ali, D. G. Braun, A. Fernandez-Pañella, S. Zhang, R. G. Kraus, F. Coppari, J. M. McNaney, M. C. Marshall, L. E. Kirch, D. C. Swift, M. Millot, J. K. Wicks, and J. H. Eggert, Probing the Solid Phase of Noble Metal Copper at Terapascal Conditions, Phys. Rev. Lett. **124**, 015701 (2020).

[16] P. M. Celliers, D. K. Bradley, G. W. Collins, D. G. Hicks, T. R. Boehly, and W. J. Armstrong, Line-imaging velocimeter for shock diagnostics at the OMEGA laser facility, Rev. Sci. Instrum. **75**, 4916 (2004).

[17] A. Dewaele, P. Loubeyre, and M. Mezouar, Equations of state of six metals above 94 GPa, Phys. Rev. B **70**, 094112 (2004).

[18] Y. Fei, A. Ricolleau, M. Frank, K. Mibe, G. Shen, and V. Prakapenka, Toward an internally consistent pressure scale, Proc. Natl. Acad. Sci. USA **104**, 9182 (2007).

[19] S. M. Dorfman, V. B. Prakapenka, Y. Meng, and T. S. Duffy, Intercomparison of pressure standards (Au, Pt, Mo, MgO, NaCl and Ne) to 2.5 Mbar, J. Geophys. Res. **117**, B08210 (2012).

[20] R. F. Smith, J. H. Eggert, R. Jeanloz, T. S. Duffy, D. G. Braun, J. R. Patterson, R. E. Rudd, J. Biener, A. E. Lazicki, A. V. Hamza *et al.*, Ramp compression of diamond to five terapascals, Nature (London) **511**, 330 (2014).

[21] D. K. Bradley, J. H. Eggert, R. F. Smith, S. T. Prisbrey, D. G. Hicks, D. G. Braun, J. Biener, A. V. Hamza, R. E. Rudd, and G. W. Collins, Diamond at 800 GPa, Phys. Rev. Lett. **102**, 075503 (2009).

[22] M. J. MacDonald, E. E. McBride, E. Galtier, M. Gauthier, E. Granados, D. Kraus, A. Krygier, A. L. Levitan, A. J. MacKinnon, I. Nam *et al.*, Using simultaneous x-ray diffraction and velocity interferometry to determine material strength in shock-compressed diamond, Appl. Phys. Lett. **116**, 234104 (2020).

[23] T. J. Vogler, T. Ao, and J. R. Asay, High-pressure strength of aluminum under quasi-isentropic loading, Int. J. Plast. **25**, 671 (2009).

[24] R. S. McWilliams, J. H. Eggert, D. G. Hicks, D. K. Bradley, P. M. Celliers, D. K. Spaulding, T. R. Boehly, G. W. Collins, and R. Jeanloz, Strength effects in diamond under shock compression from 0.1 to 1 TPa, Phys. Rev. B **81**, 014111 (2010).

[25] D. E. Fratanduono, R. F. Smith, D. G. Braun, J. R. Patterson, R. G. Kraus, T. S. Perry, A. Arsenlis, G. W. Collins, and J. H. Eggert, The effect of nearly steady shock waves in ramp compression experiments, J. Appl. Phys. **117**, 245903 (2015).

[26] D. E. Fratanduono, M. Millot, D. G. Braun, S. J. Ali, A. Fernandez-Pañella, C. T. Seagle, J. P. Davis, J. L. Brown, Y. Akahama, R. G. Kraus *et al.*, Establishing gold and platinum standards to 1 terapascal using shockless compression, Science **372**, 1063 (2021).

[27] S. M. Sharma, S. J. Turneaure, J. M. Winey, and Y. M. Gupta, What Determines the fcc-bcc Structural Transformation in Shock Compressed Noble Metals? Phys. Rev. Lett. **124**, 235701 (2020).

[28] S. K. Han, R. F. Smith, D. Kim, J. K. Wicks, J. R. Rygg, A. Lazicki, J. H. Eggert, and T. S. Duffy, Polymorphism of gold under laser-based ramp compression to 690 GPa, Phys. Rev. B **103**, 184109 (2021).

[29] R. G. Kraus, F. Coppari, D. E. Fratanduono, R. F. Smith, A. Lazicki, C. Wehrenberg, J. H. Eggert, J. R. Rygg, and G. W. Collins, Melting of Tantalum at Multimegabar Pressures on the Nanosecond Timescale, Phys. Rev. Lett. **126**, 255701 (2021).

[30] J. A. Moriarty, Ultrahigh-pressure structural phase transitions in Cr, Mo, and W, Phys. Rev. B **45**, 2004 (1992).

[31] A. L. Ruoff and C. Rodriguez, Elastic moduli of tungsten to 15 Mbar, phase transition at 6.5 Mbar, and rheology to 6 Mbar, Phys. Rev. B **58**, 2998 (1998).

[32] J. H. Eggert, R. F. Smith, D. C. Swift, R. E. Rudd, D. E. Fratanduono, D. G. Braun, J. A. Hawreliak, J. M. McNaney, and G. W. Collins, Ramp compression of tantalum to 330 GPa, High Press. Res. **35**, 339 (2015).

[33] J. Eggert, M. Bastea, D. B. Reisman, S. Rothman, J. P. Davis, M. D. Knudson, D. B. Hayes, G. T. Gray, D. Erskine, and G. W. Collins, Ramp wave stress-density measurements of Ta and W, AIP Conf. Proc. **955**, 1177 (2007).

[34] T. R. Boehly, D. L. Brown, R. S. Craxton, R. L. Keck, J. P. Knauer, J. H. Kelly, T. J. Kessler, S. A. Kumpan, S. J. Loucks, S. A. Letzring *et al.*, Initial performance results of the OMEGA laser system, Opt. Commun. **133**, 495 (1997).

[35] F. Coppari, R. F. Smith, D. B. Thorn, J. R. Rygg, D. A. Liedahl, R. G. Kraus, A. Lazicki, M. Millot, and J. H. Eggert, Optimized x-ray sources for x-ray diffraction measurements at the Omega Laser Facility, Rev. Sci. Instrum. **90**, 125113 (2019).

[36] J. R. Maw, A characteristics code for analysis of isentropic compression experiments, AIP Conference Procedings **706**, 1217 (2004).

[37] S. D. Rothman and J. Maw, Characteristics analysis of isentropic compression experiments (ICE), J. Phys. IV France **134**, 745 (2006).

[38] J. K. Wicks, R. F. Smith, D. E. Fratanduono, F. Coppari, R. G. Kraus, M. G. Newman, J. R. Rygg, J. H. Eggert, and T. S. Duffy, Crystal structure and equation of state of Fe-Si alloys at super-Earth core conditions, Sci. Adv. **4**, eaao5864 (2018).

[39] E. Raub, H. Beeskow, and D. Menzel, Tantal-Gold-Legierungen, Z. Metallkd. **52**, 189 (1961).

[40] H. Luo, Superconductivity and lattice parameters in face-centered cubic Pt-W and Pd-W solid solutions, J. Less-Common Met. **15**, 299 (1968).

[41] H. Mehrer, *Diffusion in Solids. Fundamentals, Methods, Materials, Diffusion-Controlled Processes* (Springer, New York, 2007).

[42] T. Mashimo, X. Liu, M. Kodama, E. Zaretsky, M. Katayama, and K. Nagayama, Effect of shear strength on Hugoniot-compression curve and the equation of state of tungsten (W), J. Appl. Phys. **119**, 035904 (2016).

[43] R. G. Kraus, R. J. Hemley, S. J. Ali, J. L. Belof, L. X. Benedict, J. Bernier, D. Braun, R. E. Cohen, G. W. Collins, F. Coppari *et al.*, Measuring the melting curve of iron at super-earth core conditions, Science **375**, 202 (2022).

[44] R. F. Smith, D. E. Fratanduono, D. G. Braun, T. S. Duffy, J. K. Wicks, P. M. Celliers, S. J. Ali, A. Fernandez-pañella, R. G. Kraus, D. C. Swift *et al.*, Equation of state of iron under core conditions of large rocky exoplanets, Nat. Astron. **2**, 452 (2018).

[45] A. Dewaele, M. Torrent, P. Loubeyre, and M. Mezouar, Compression curves of transition metals in the Mbar range: Experiments and projector augmented-wave calculations, Phys. Rev. B **78**, 104102 (2008).

[46] S. J. Turneaure, S. M. Sharma, and Y. M. Gupta, Crystal Structure and Melting of Fe Shock Compressed to 273 GPa: *In Situ* X-Ray Diffraction, Phys. Rev. Lett. **125**, 215702 (2020).

[47] J. Wang, F. Coppari, R. F. Smith, J. H. Eggert, A. E. Lazicki, D. E. Fratanduono, J. R. Rygg, T. R. Boehly, G. W. Collins, and T. S. Duffy, X-ray diffraction of molybdenum under ramp compression to 1 TPa, Phys. Rev. B **94**, 104102 (2016).

[48] R. E. Cohen and O. Gülseren, Thermal equation of state of tantalum, Phys. Rev. B **63**, 224101 (2001).

[49] K. D. Litasov, P. N. Gavryushkin, P. I. Dorogokupets, I. S. Sharygin, A. Shatskiy, Y. Fei, S. V. Rashchenko, Y. V. Seryotkin, Y. Higo, K. Funakoshi, and E. Ohtani, Thermal equation of state to 33.5 GPa and 1673 K and thermodynamic properties of tungsten, J. Appl. Phys. **113**, 133505 (2013).